

# X-ray variability in a deep, flux limited sample of QSOs

O. Almaini,<sup>1</sup> A. Lawrence,<sup>1</sup> T. Shanks,<sup>2</sup> A. Edge,<sup>2</sup> B.J. Boyle,<sup>3</sup> I. Georgantopoulos,<sup>4</sup> K.F. Gunn,<sup>5</sup> G.C. Stewart,<sup>6</sup> and R.E. Griffiths<sup>7</sup>

<sup>1</sup> *Institute for Astronomy, Royal Observatory, University of Edinburgh, Blackford Hill, Edinburgh EH9 3HJ*

<sup>2</sup> *Department of Physics, University of Durham, South Road, Durham DH1 3LE*

<sup>3</sup> *Anglo-Australian Observatory, PO Box 296, Epping NSW 2121, Australia*

<sup>4</sup> *National Observatory of Athens, I. Metaxa & B. Pavlou, Palaia Penteli, 15236, Athens, Greece*

<sup>5</sup> *Department of Physics & Astronomy, University of Southampton, University Road, Southampton SO17 1BJ*

<sup>6</sup> *Department of Physics and Astronomy, The University of Leicester, Leicester LE1 7RH*

<sup>7</sup> *Department of Physics, Carnegie Mellon University, Wean Hall, 5000 Forbes Ave., Pittsburgh, PA 15213, USA*

MNRAS in press

## ABSTRACT

We present an analysis of X-ray variability in a flux limited sample of QSOs. Selected from our deep ROSAT survey, these QSOs span a wide range in redshift ( $0.1 < z < 3.2$ ) and are typically very faint, so we have developed a method to constrain the amplitude of variability in ensembles of low signal-to-noise light curves. We find evidence for trends in this variability amplitude with both redshift and luminosity. The mean variability amplitude declines sharply with luminosity, as seen in local AGN, but with some suggestion of an upturn for the most powerful sources. We find tentative evidence that this is caused by redshift evolution, since the high redshift QSOs ( $z > 0.5$ ) do not show the anti-correlation with luminosity seen in local AGN. We speculate on the implications of these results for physical models of AGN and their evolution. Finally, we find evidence for X-ray variability in an object classified as a narrow emission-line galaxy, suggesting the presence of an AGN.

**Key words:** galaxies: active – galaxies:evolution- – galaxies:nuclei- – quasars: general - X-rays: general – X-rays: galaxies

## 1 INTRODUCTION

The X-ray flux from AGN exhibits variability on shorter timescales than any other waveband, indicating that this emission occurs in the innermost region of the central engine. Detailed studies of X-ray variability can therefore act as important probes of the AGN phenomenon, potentially yielding information on size scales unresolvable by any other means.

While previous observations had revealed that X-ray variability was very common in AGN (see Mushotzky, Done & Pounds 1993 for a review), the most significant advances were made with the ‘long look’ observations taken with the *EXOSAT* observatory. The highly eccentric orbit of this satellite combined with its much improved sensitivity allowed continuous observations of a small number of local AGN with high signal to noise. The light curves appeared very random in nature. Fourier and spectral analyses revealed no preferred timescales or periodicities. Instead these sources showed power smoothly distributed over a wide range of frequencies, generally with power spectra of the form  $P(f) \propto f^{-1.5}$  (Lawrence & Papadakis 1993, Green et al 1993). Such light curves are described as *red noise*, i.e. scale free but with more power at low frequencies. The power spectra are eventually expected to flatten from a power-law form at the lowest frequencies below  $\sim 10^{-6}$  Hz (Edelson et al 1999). Similarly, at high frequen-

cies we expect a cutoff corresponding to the smallest scales in the emitting region (e.g. the inner region of the accretion disk) but so far no such steepening has been observed.

Interesting results were obtained by comparing the variability in different AGN, suggesting that more luminous sources vary with lower amplitude. Barr & Mushotzky (1986) studied the shortest timescale required for a source to double in flux and observed an increase in the doubling timescale with luminosity. Lawrence & Papadakis (1993) and Green et al (1993) studied the power spectra of the *EXOSAT* AGN and found that the power at a given frequency decreases with luminosity with the form  $P \propto L_x^{-(0.6 \pm 0.1)}$ . This result has since been confirmed by observations with the *ASCA* satellite, albeit with overlapping samples of AGN (Nandra et al 1997, Turner et al 1999). Such trends might be explained if more luminous sources are physically larger in size. However, these studies were conducted on a small number of bright AGN at low redshift ( $z < 0.1$ ). Since QSO activity is known to have peaked at much earlier epochs ( $z \simeq 2$ ) it is now vital to establish whether the trends observed in these local AGN apply to the QSO population as a whole and to test for evolutionary effects. In this work we present an analysis of a flux limited sample of 86 QSOs detected as part of the Deep ROSAT Survey (Georgantopoulos et al 1996). Spanning a wide range in redshift ( $0.1 < z < 3.2$ ), the

same sample has been used to define the form and evolution of the QSO luminosity function (Boyle et al 1994). Most of the sources are detections at the faintest possible X-ray flux and hence the light curves are generally of low signal to noise. Nevertheless, we have developed methods for constraining the level of intrinsic variability in each source. By combining the results from many QSOs we can search for trends in the typical variability amplitude with redshift and luminosity. Finally we study the variability of X-ray emitting galaxies to test the hypothesis that these contain obscured AGN.

## 2 THE SAMPLE

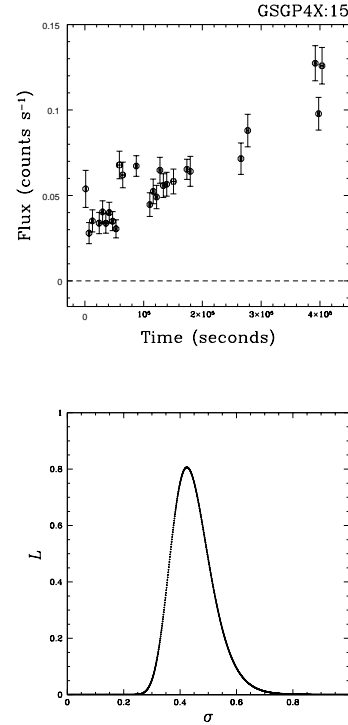
Our sample consists of 86 QSOs identified during the Deep *ROSAT* Survey of Shanks et al (in preparation), which reached an X-ray flux limit of  $\sim 4 \times 10^{-15} \text{ erg s}^{-1} \text{ cm}^{-2}$  (0.5-2.0 keV). A description of the X-ray source detection and optical identification is given in Georgantopoulos et al (1996). Details of the QSO redshift distribution and the X-ray luminosity function and its evolution are given in Boyle et al (1994).

The survey uses 7 deep *ROSAT* PSPC pointings, with integration times of  $\sim 30 - 80$  ks per field, spread over periods ranging from 2-14 days. Periodic gaps in the light curves are caused by the orbit of the satellite, with larger gaps occurring during phases of high instrument background, such as when the satellite passes through the South Atlantic Anomaly. During each 96 minute orbit, a source is typically visible for 1000 – 2000 seconds. Given the faint nature of the X-ray sources, light curves were first binned on these periodic orbits, giving 16 – 26 observation slots (depending on the field). The fainter sources are then re-binned to allow meaningful Gaussian statistics. Using the mean intensity of the source, if the smallest bin is expected to give fewer than 20 photons it is merged with its nearest neighbour. This process is repeated until  $\bar{I}\Delta t > 20$  photons per bin, leaving 86 QSOs with an absolute minimum of at least 2 time bins. We note that this re-binning process will inevitably smear out high frequency variability, and discuss this effect further in Section 3 and Appendix A.

Basic data reduction was carried out using the *Asterix* X-ray data processing package. For each source, depending on the off-axis radius, a source box radius was chosen to enclose 90 per cent of the X-ray photons. Assuming a mean QSO spectral index of  $\Gamma = 2.2$  (Almaini et al 1996), the radius of this circle varies from  $24.6''$  on axis to  $56.6''$  at a maximum radius of 18 arcmin. Data from periods of high particle background are excluded from the analysis. This removes  $\sim 10$  per cent of the data when the Master Veto Rate rises above  $170 \text{ counts s}^{-1}$  (Plucinsky et al 1993). Considerable care was taken in choosing areas for background subtraction. By good fortune, none of the fields showed evidence for significant background gradients (generally caused by irregularities in the galactic background or contamination from solar scattered X-rays). Typically 10 circular areas of 4-6 arcmin radius are then chosen across each field from source free regions to perform the background subtraction. The background box closest to each source was used, with minor vignetting corrections ( $< 5$  per cent) to correct for the differing off axis radii of source and background boxes.

Problems may also conceivably arise if the background shows differing variability across the field. Although care is taken to use background regions close to each source, differential variability may nevertheless introduce extra variance into the light curves above the Poisson noise and bias the results. Some of the fields do indeed show evidence for variability at a low level ( $\delta I/I < 10$  per

**Figure 1.** Light curve and likelihood function (of arbitrary normalisation) for the QSO GSGP4X:015



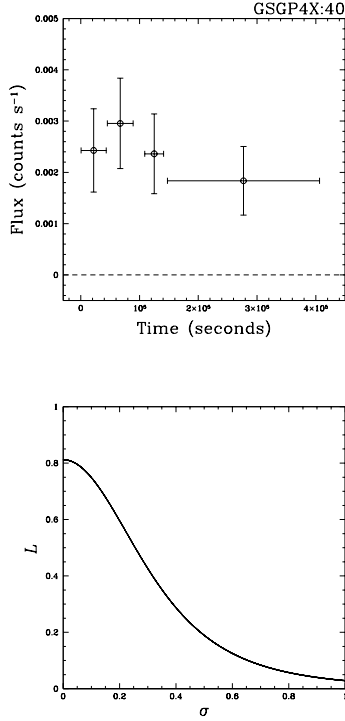
cent), probably due to contamination from solar scattered X-rays, but this is consistent across the detector. Such minor effects will therefore be removed in background subtraction. Finally, to check that any variability was real and not due to a flickering response in the PSPC, we compared the light curves of brighter QSOs with each other and with background regions. No significant correlations could be seen, suggesting that the bulk of the variability is indeed real and not caused by mysterious instrumental effects.

## 3 MEASURING THE AMPLITUDE OF QSO VARIABILITY

We now develop a method for measuring the amplitude of intrinsic fluctuations in light curves of low signal to noise. Although many will be too faint to enable a significant detection of variability, we can nevertheless place upper limits on the amplitude of fluctuations which could be present. In order to combine information from faint light curves, we will also extend this method to measure the typical variability in an ensemble of QSOs (e.g. within a given luminosity or redshift range).

Unlike the well studied *EXOSAT* light curves, the QSOs studied here are too faint to obtain variability amplitudes by detailed power spectrum analysis. A simpler method is to estimate the intrinsic variance in the light curve. Since this quantity is proportional to the amplitude of the power spectrum (see Appendix A) it will also allow comparisons with previous work. Nandra et al (1997) used the root mean square variation in their *ASCA* lightcurves, subtracting off a contribution due to noise. An intrinsic assumption in this method is that each point in the light curve has equal weight, which will break down in cases where the errors differ significantly from point to point. We therefore develop a new

**Figure 2.** Light curve and likelihood function (of arbitrary normalisation) for the QSO GSGP4X:040



maximum likelihood technique to extract the best estimate of the intrinsic (noise subtracted) variance given a set of data values  $x_i$  with differing measurement errors  $\sigma_i$ .

In order to compare objects of different flux in a meaningful way, all light curves are first divided by their mean flux. Hence we are measuring the amplitude of *fractional* variability. When an ensemble of QSOs is considered (e.g. all QSOs within a given redshift range) we treat each light curve as a ‘snapshot’ from the population and assume that the ensemble all have the same underlying distribution in  $I/\bar{I}$ . By definition the variance does not depend on the ordering of the points and hence we can combine the light curves and measure the variance in the resulting distribution. We now describe a method for separating the intrinsic variance from the scatter due to measurement errors.

### 3.1 A maximum likelihood estimator

The variance in a light curve has two components: first there will be fluctuations due to noise ( $\sigma_{noise}^2$ ) and secondly there may be intrinsic variations from the QSO or ensemble of QSOs ( $\sigma_Q^2$ ). Hence:

$$\sigma_{total}^2 = \sigma_{noise}^2 + \sigma_Q^2 \quad (1)$$

If we assume Gaussian statistics, for a light curve with mean  $\bar{x}$  and measurement errors  $\sigma_i$ , the probability density for obtaining the  $N$  data values  $x_i$  is given by:

$$p(x_i|\sigma_i, \sigma_Q) = \prod_{i=1}^N \frac{\exp\left\{-\frac{1}{2}(x_i - \bar{x})^2/(\sigma_i^2 + \sigma_Q^2)\right\}}{(2\pi)^{1/2}(\sigma_i^2 + \sigma_Q^2)^{1/2}} \quad (2)$$

This is simply a product of  $N$  Gaussian functions representing the probability distribution for each bin. We may turn this around

using Bayes’ Theorem to obtain the probability distribution for  $\sigma_Q$  given our measurements:

$$p(\sigma_Q|x_i, \sigma_i) = p(x_i|\sigma_i, \sigma_Q) \frac{p(\sigma_Q)}{p(x_i)} \quad (3)$$

$$\propto L(\sigma_Q|x_i, \sigma_i) \quad (4)$$

where  $L(\sigma_Q|x_i, \sigma_i)$  is the likelihood function for the parameter  $\sigma_Q$  given the data. This general form for the likelihood function can be calculated if one assumes a Bayesian prior distribution for  $\sigma_Q$  and  $x_i$ . In the simplest case of a uniform prior one obtains:

$$L(\sigma_Q|x_i, \sigma_i) \propto p(x_i|\sigma_i, \sigma_Q) \quad (5)$$

$$= \prod_{i=1}^N \frac{\exp\left\{-\frac{1}{2}(x_i - \bar{x})^2/(\sigma_i^2 + \sigma_Q^2)\right\}}{(2\pi)^{1/2}(\sigma_i^2 + \sigma_Q^2)^{1/2}} \quad (6)$$

By differentiating the above, the maximum likelihood estimate for  $\sigma_Q$  can be shown to satisfy the following, which (for a uniform prior) is mathematically identical to a least  $\chi^2$  solution:

$$\sum_{i=1}^N \frac{\{(x_i - \bar{x})^2 - (\sigma_i^2 + \sigma_Q^2)\}}{(\sigma_i^2 + \sigma_Q^2)^2} = 0 \quad (7)$$

In the case of zero measurement errors, this reduces to the standard form:

$$\lim_{\sigma_i \rightarrow 0} \sigma_Q^2 = \sum_{i=1}^N (x_i - \bar{x})^2 / N \quad (8)$$

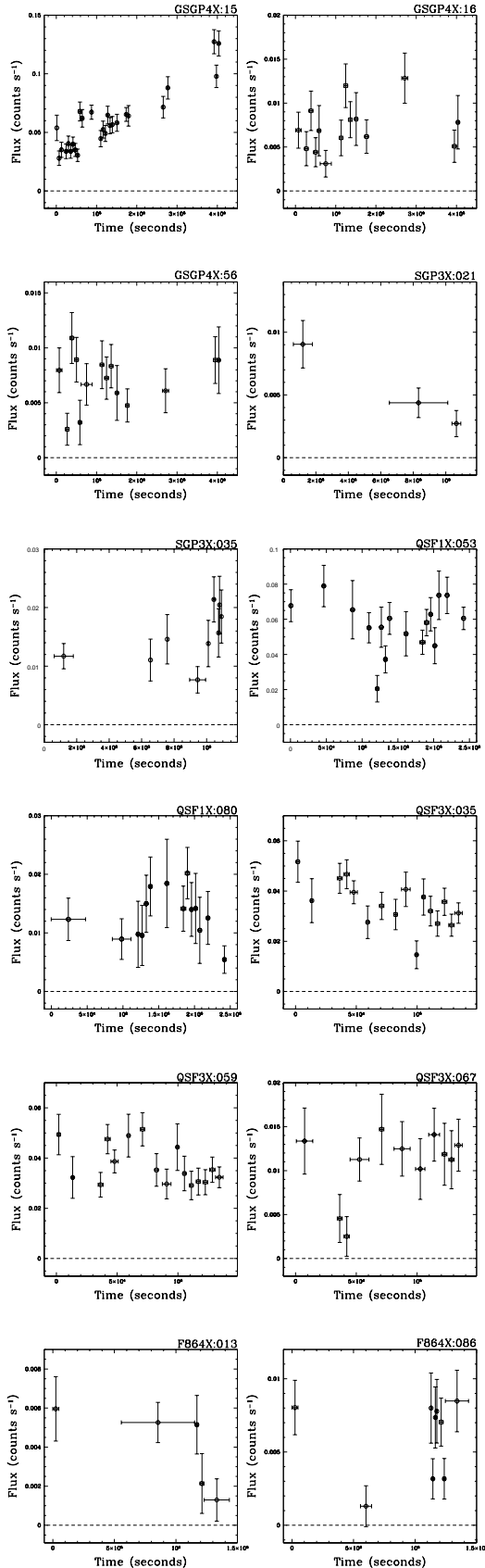
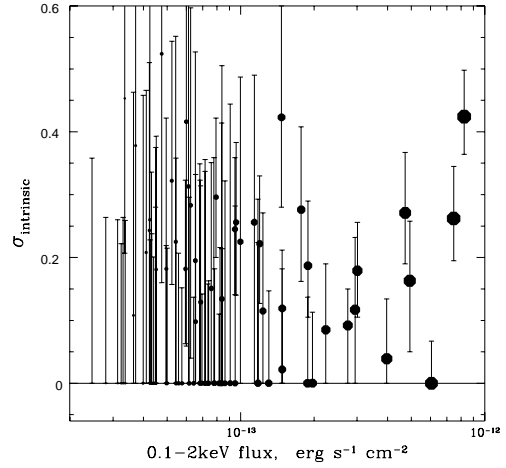
In the case of identical measurement errors ( $\sigma_m = constant$ ) this reduces to the form used by Nandra et al (1997):

$$\lim_{\sigma_i \rightarrow \sigma_m} \sigma_Q^2 = \sum_{i=1}^N \{(x_i - \bar{x})^2 - \sigma_m^2\} / N \quad (9)$$

In general however, Equation 7 can only be solved analytically for the case where  $N \leq 2$ . For a larger number of bins we must find the maximum likelihood estimate numerically. Two contrasting examples of light curves and their likelihood functions are given in Figures 1 and 2, from QSOs of high and low flux respectively. From these, maximum likelihood estimates for  $\sigma_Q$  can be evaluated with suitable error bounds. The maximum likelihood estimate for  $\sigma_Q$  is obtained by locating the peak of the likelihood curve, while the error bounds are obtained in the standard way by assuming that the likelihood curve has a Gaussian shape.

This method can either be applied to individual light curves or an ensemble. In comparing values of  $\sigma_Q$ , however, it is important to be aware of the effects of different total integration times and sampling. In addition, one might expect cosmological time dilation to modify the results. A detailed examination of these effects can be found in Appendices A & B. We find that one can apply a correction to allow for these changes, but only under the assumption of a particular underlying power spectrum. We therefore carried out our analysis with and without these timescale corrections, but overall we found that they have no significant effect on the results.

## 4 THE RESULTS

**Figure 3.** Light curves of the 12 QSOs showing evidence for variability with > 95 per cent significance.**Figure 4.** Showing the maximum likelihood estimates for the intrinsic variability as a function of flux for the 86 QSOs. Timescale corrections have not been applied. The point size is proportional to the object flux, to aid in distinguishing objects of higher S/N in Figures 5, 6, 8 and 9.

#### 4.1 Detecting individually variable QSOs

Before applying the maximum likelihood technique, a simple  $\chi^2$  test was performed on each light curve to test for variability against the null hypothesis that the flux remains constant:

$$\chi^2 = \sum_n \frac{[I_n - \langle I_n \rangle]^2}{\langle \sigma_n^2 \rangle} \quad (10)$$

The results show that only 12 of the 86 QSOs show individual evidence for variability with a significance > 95 per cent, of which 4 are significant at > 99 per cent. The light curves for these QSOs are displayed in Figure 3. As expected, the fraction of significantly variable objects increases at higher flux. Of the 10 brightest QSOs for example, 5 show variability at > 95 per cent significance, with a further 2 showing variability at a significance of 90 per cent, suggesting that a large fraction of all QSOs would show variability given sufficient signal-to-noise.

It is important to emphasise that the non-detection of variability in the remaining QSOs does not imply that no variability is occurring. Any intrinsic variations which are present are simply overwhelmed by photon noise. The detection of significant variability depends on the amplitude of intrinsic fluctuations and on the signal to noise. Since we can measure the photon noise, it should therefore be possible to at least place an upper limit on the amplitude of intrinsic fluctuations in every QSO. Only then can we make quantitative statements about the “typical” variability in the population.

#### 4.2 The maximum likelihood results

Numerically solving Equation 7 for each of the 86 QSOs, the maximum likelihood estimates for the intrinsic variability amplitude are displayed in Figure 4 (with 68 per cent confidence regions), plotting  $\sigma$  as a function of flux. The timescale corrections outlined in Appendix A are not applied to these raw data points, but these have no major effect on the results (see below). As expected, for most faint QSOs individually we can only estimate upper limits for the variability amplitude, but nevertheless the brighter QSOs and the

**Figure 5.** (a) Maximum likelihood estimates for the variability amplitude as a function of luminosity for the 86 QSOs. The point size is proportional to the object flux (see Figure 4) in order to highlight objects with higher S/N. In (b) we display the results in ensemble form, with unfilled squares showing the minor effect of not applying timescale corrections.

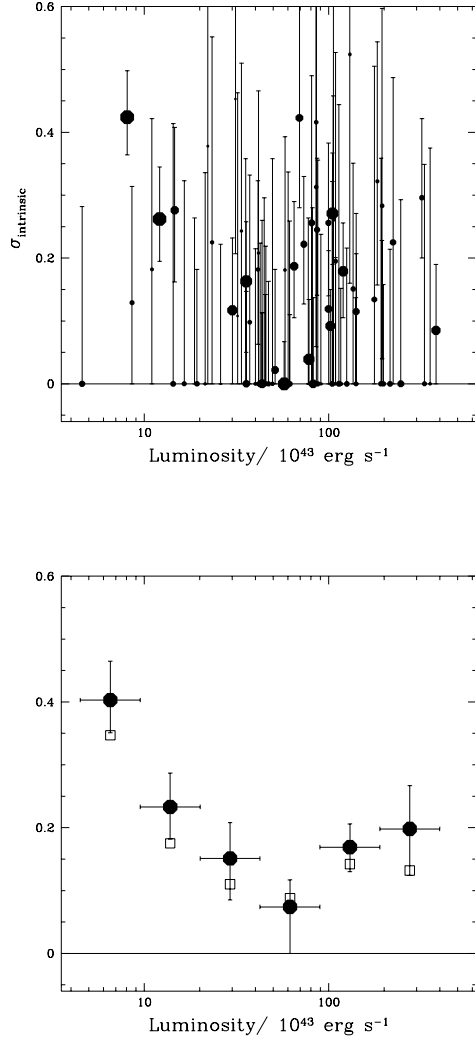
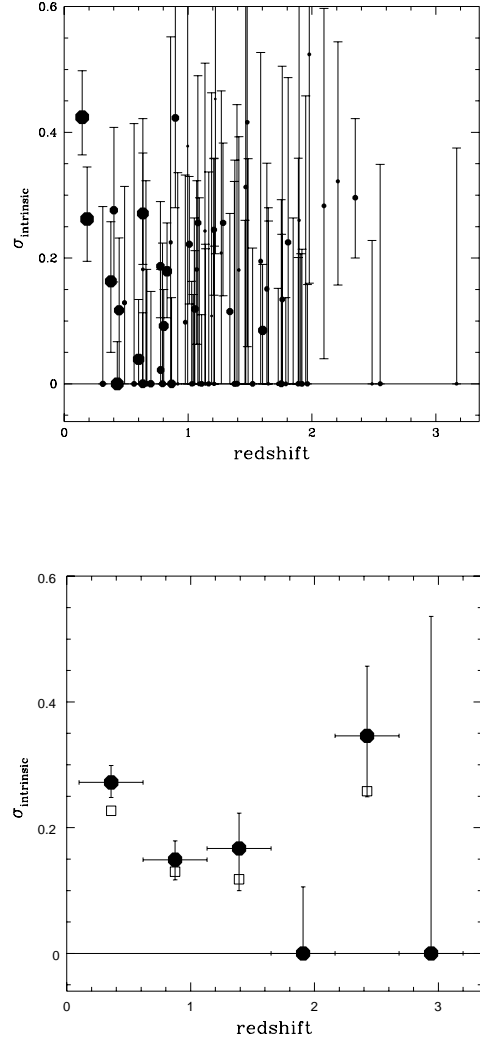


**Figure 6.** (a) Maximum likelihood estimates for the variability amplitude as a function of redshift for the 86 QSOs. The point size is proportional to the object flux (see Figure 4) in order to highlight objects with higher S/N. In (b) we display the results in ensemble form, with unfilled squares showing the minor effect of not applying timescale corrections.



fainter objects combined would seem to suggest a typical variability amplitude significantly above zero (with  $\bar{\sigma} \sim 0.2$ ).

In Figures 5(a) & 6(a) we display the variability amplitude as a function of luminosity and redshift. We split the data into 6 equally spaced luminosity and redshift bins and measure the ensemble variance, applying the same maximum likelihood technique to the combined light curves (Figure 5(b) and 6(b)). The ensemble results are displayed with and without the timescale corrections, which are dependent on the assumed power spectrum. Although the net effect of these corrections is to boost  $\sigma$  upwards, they clearly have no significant effect on the results.

We find a clear detection of variability in the ensemble of QSOs, with evidence for trends with luminosity and redshift. A  $\chi^2$  test was applied to test the null hypothesis that the scatter in the 5 points on Figures 5(b) and 6(b) is consistent with their error

bounds. For both the redshift and luminosity data, we can reject the null hypothesis with  $> 99$  per cent confidence.

### 4.3 Correlations With Redshift And Luminosity

Previous studies of very local ( $z < 0.1$ ) AGN found significant evidence for a relationship variability amplitude and luminosity, parameterised by the form  $\sigma^2 \propto L_x^{-(0.6 \pm 0.1)}$  (Lawrence & Papadakis 1993, Green & McHardy 1993, Nandra et al 1997). In Figure 7 we compare our ensemble QSO results with the work of Papadakis & Lawrence (1993) and Nandra et al (1997) (although we note that there is considerable overlap between these local samples). Similar results have recently been found by Turner et al (1999). To allow a meaningful comparison we convert luminosities to our 0.1 – 2 keV band (assuming a spectral shape of the form  $\alpha = 1.0$  above 1 keV and  $\alpha = 1.5$  below 1 keV). Values of  $\sigma$  were cor-

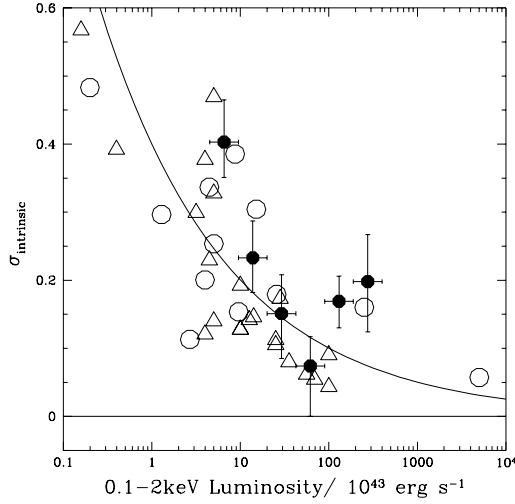


**Figure 7.** A comparison of the *ROSAT* results with the findings of Lawrence & Papadakis (1993) (circles) and Nandra et al (1997) (triangles). The best fitting power-law of the form  $\sigma^2 \propto L_x^{-0.6}$  is shown (not fitted to the *ROSAT* QSOs). To allow a crude comparison, values of  $\sigma$  have been normalised to timescales below 1 week using a temporal power spectrum of the form  $f^{-1.5}$  and luminosities have been converted to the 0.1 – 2 keV band.

rected to timescales of 1 week (assuming a power spectrum of the form  $P(f) \propto f^{-1.5}$ ). Given the uncertainties in these conversions, and the fact that previous variability studies were conducted at higher X-ray energies, we will be cautious in making direct comparisons. However, we note that the amplitudes found in our QSOs are broadly consistent with these local AGN. This would support the hypothesis that the driving force in any variability trend is actually the QSO luminosity, rather than the redshift. Formally, however, a power-law gives a very poor fit to the data (see Table 1).

An intriguing result is the apparent minimum at  $L_x \sim 5 \times 10^{44} \text{ erg s}^{-1}$ , with an upturn towards higher luminosities. No evidence for such an upturn has been seen among local AGN. To allow a fairer comparison, we split our sample into ‘local’ and ‘distant’ QSOs, dividing at  $z = 0.5$  (Figures 8,9). We find that while the local QSOs show a clear anti-correlation with luminosity, consistent with previous studies, the QSOs at higher redshift show no evidence for this trend whatsoever. To parameterise this difference, we perform power-law fits to these distributions (see Table 1; similar results are obtained if we fit to the binned, ensemble data). Unlike the full sample, we find that a power-law can describe these separate distributions well ( $\chi_{red}^2 \sim 1$ ) and we obtain good fits with  $\sigma^2 \propto L_x^{-(1.5 \pm 0.2)}$  for the low redshift QSOs but a very different form for the higher redshift objects, with  $\sigma^2 \propto L_x^{+(0.6 \pm 0.3)}$  (i.e. a possible *positive* correlation with luminosity). There is a strong degeneracy between luminosity and redshift, however, and it would clearly be desirable to obtain a larger sampling of the  $L - z$  plane. If one restricts the comparison to only the 3 overlapping luminosity bins, for example, a  $\chi^2$  test rejects the hypothesis that the two distributions are the same at only the 95 per cent confidence level. We therefore urge caution in over-interpreting these results, but we will explore some of the possible consequences in Section 5.4.

**Table 1.** Showing power-law fits to the distribution of  $\sigma^2$  vs luminosity for the *ROSAT* QSOs.

Data	Best fit	$\chi_{red}^2$
All QSOs	$\sigma^2 \propto L_x^{-(0.8 \pm 0.2)}$	2.5
$z < 0.5$	$\sigma^2 \propto L_x^{-(1.5 \pm 0.2)}$	1.2
$z > 0.5$	$\sigma^2 \propto L_x^{+(0.6 \pm 0.3)}$	0.8

## 5 CONSTRAINING PHYSICAL MODELS

Although we find some evidence for an upturn in the  $\sigma/L_x$  relation at high luminosities, it is now well established that a strong anti-correlation exists between these two parameters, at least for local AGN. We will now explore some possible physical implications of this trend, returning to the possible consequences of an upturn in Section 5.4.

The most plausible explanation for the observed anti-correlation is that high luminosity sources have larger emitting regions. It is currently unclear whether this is due to a single, coherent but erratically varying source or a large number of independent flaring regions (Abramowicz et al 1991). The incoherence in the light curves of *EXOSAT* AGN would suggest a stochastic random process governed by a large number of variables (Krolik, Done & Madejski 1993), as would the lack of any obvious timescale (Lawrence et al 1987). We now investigate how the observed relation  $\sigma^2 \propto L_x^{-(0.6 \pm 0.1)}$  can be used to constrain two classes of models for AGN variability and in turn discuss the implications for QSO evolutionary models.

### 5.1 The single coherent oscillator

In the case where the X-ray variability is caused by global, coherent changes in the emitting region, it is reasonable to assume that the luminosity of the source will be related to its physical size. The geometry of the emitting region is unclear however, and could be spherical, disk shaped etc., and hence we assume a general relationship between the X-ray luminosity and the characteristic radius,  $R$ :

$$L_x \propto R^\beta \quad (11)$$

Over the range of frequencies we are interested in, we will assume a temporal power spectrum of the form  $P(f) \propto f^{-\alpha}$  (where  $\alpha \simeq 1.5$ ) as observed in local AGN (Lawrence & Papadakis 1993). Assuming self similar scaling, timescales will be scaled in direct proportion to the size of the source, and hence in larger sources the temporal power spectrum will simply be shifted in the frequency direction. Self similar scaling requires conservation of the total integrated fractional power, but the power measured over a narrow frequency range will change. By integrating the new power spectrum over the observed frequency range one can relate the *observed* variance to the size of the source:

$$\sigma^2 = \int_{f_1}^{f_2} P(f) df \quad (12)$$

$$\propto f_1^{1-\alpha} \quad (f_1 \ll f_2, \alpha \neq 1) \quad (13)$$

$$\propto R^{1-\alpha} \quad (14)$$

$$\propto L_x^{(1-\alpha)/\beta} \quad (15)$$

Thus one can readily reproduce the observed anti-correlation with luminosity ( $\sigma^2 \propto L_x^{-(0.6 \pm 0.1)}$ ) given the measured power

**Figure 8.** (a) Variability amplitude as a function of luminosity for the low redshift ( $z < 0.5$ ) QSOs. In (b) we display the results in ensemble form.

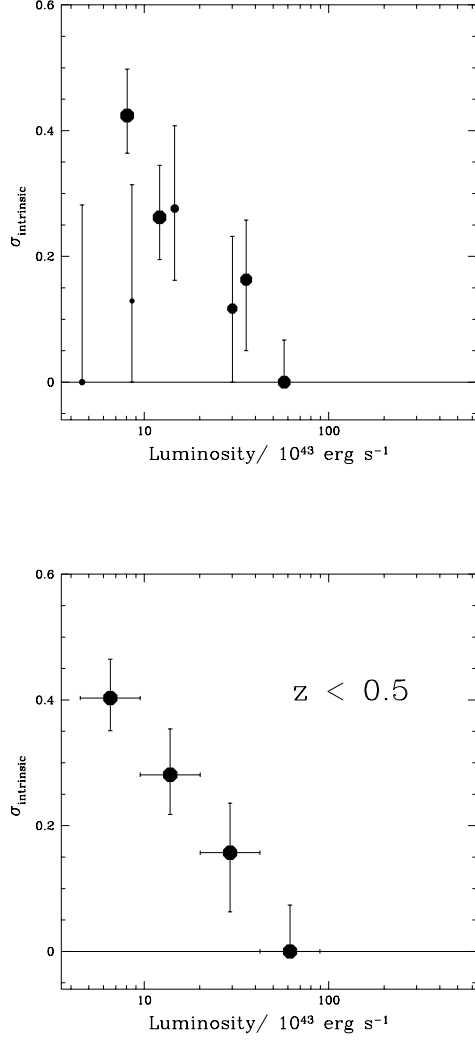
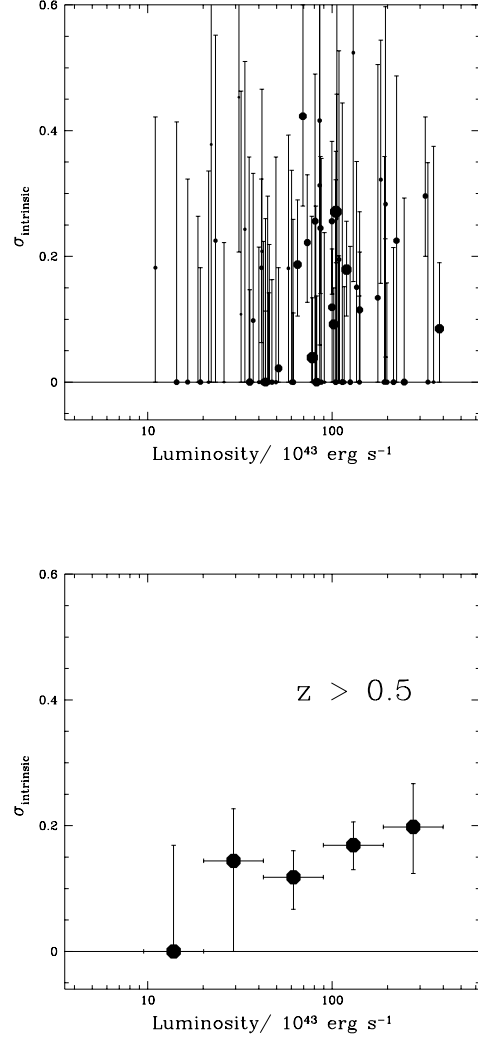


**Figure 9.** (a) Variability amplitude as a function of luminosity for the high redshift ( $z > 0.5$ ) QSOs. In (b) we display the results in ensemble form.



spectrum slope ( $\alpha \simeq 1.5$ ) if the geometry of the source is such that  $L_x \propto R^{0.7-1.0}$ . This would be consistent with a ring of X-ray emitting material rather than a disk or spherical cloud. We note, however, that alternative geometries could also reproduce the observations if we allow a radial decline in the X-ray emissivity (e.g. free-free emission in a spherical cloud of material if the electron density falls off at large radii). In conclusion therefore, the observed anti-correlation can be reproduced in this model and in principle could be used to constrain the geometry of the emitting material.

## 5.2 The independent hot spot model

In this class of model, the variability is caused by independent flaring events. More luminous sources will simply have more flaring regions and hence the r.m.s. fluctuations will be smaller. If the time-averaged luminosity from each flare is  $\bar{l}$ , the typical number of flares at a given time will be related to the total X-ray luminosity,  $L_x$  by:

$$N = L_x / \bar{l} \quad (16)$$

Thus the fractional r.m.s. variation on the number of flares at a given time will be:

$$\sigma = \sqrt{N} / N \propto \left( \frac{L_x}{\bar{l}} \right)^{-0.5} \quad (17)$$

If the flares are the same size in all QSOs, this would lead to  $\sigma^2 \propto L_x^{-1}$ , which is somewhat steeper than the observed correlation. This could be overcome if higher luminosity objects had more luminous flares, such that  $\bar{l} \propto L_x^{0.5}$ . Hence this model can also explain the observed anti-correlation.

## 5.3 Constraining models of QSO evolution

As outlined in Boyle et al (1987) there are at least two possible models which can explain the strong evolution in the QSO luminosity function:

- (i) The evolution of successive generations of short lived ( $\sim$

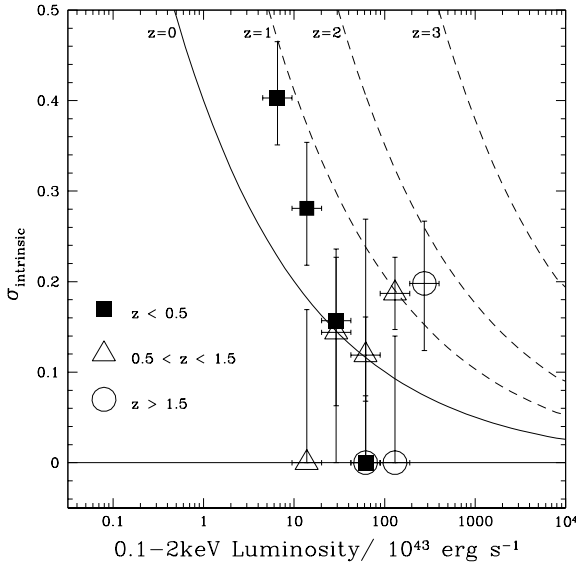


**Figure 10.** Comparison with the predictions of a long-lived single oscillator model. The local trend between variability amplitude and source luminosity ( $\sigma^2 \propto L_x^{-0.6}$ ; solid line - see Figure 8) is evolved to predict the relationship at high redshift (dashed lines). For comparison, the ROSAT QSOs are superimposed, split into 3 redshifts ranges.

$10^8$ yr) QSOs in which the mean intensity of QSO cycles diminishes. In this scenario most galaxies have been through a quasar epoch at least once.

(ii) The evolution of individual, long-lived QSOs which uniformly dim over time. In this scenario only  $\sim 1\%$  of galaxies have ever undergone quasar activity, but would develop very massive black holes.

In the first model, we expect a typical QSO to harbour a black hole of mass  $\sim 1 \times 10^8 M_\odot$  regardless of redshift. Black holes of this size allow the theoretically favoured accretion at Eddington limit (Rees 1984) for a QSO at peak activity. Thus the size of a typical emitting region is expected to be very similar at all redshifts.

In the more controversial long-lived model, QSOs have poured out a vast amount of energy over most of the age of the universe and should therefore develop extremely massive black holes by the associated accretion. This can be calculated by integrating the total energy emitted by the QSO from its formation until the present day (full details given in Appendix C). If we assume an accretion efficiency  $\varepsilon = 0.1$  after Rees (1984), an initial mass given by the Eddington limit and a starting redshift of  $z = 3$  then we predict a factor  $\sim 20h_{50}^{-1}$  increase in black hole mass from  $z = 3$  to  $z = 2$ , with a further growth by a factor of  $\sim 3h_{50}^{-1}$  from  $z = 2$  to the present day (Figure C1).

In principle therefore, since variability traces the size scales in the central regions of an AGN, one might be able to distinguish between these models. The consequences depend on the variability model:

**Single Coherent Oscillator:** In this case, the amplitude of variability is directly related to the physical size of the source (Equation 14). The X-ray emission from AGN is generally thought to arise a few Schwarzschild radii from the central black hole, and

in this metric the central mass is directly proportional to the size scale. Hence one can relate the amplitude of variability to the central black hole mass,  $M_{BH}$ :

$$\sigma^2 \propto R^{1-\alpha} \propto M_{BH}^{-0.5} \quad (18)$$

In the long-lived model this would lead to dramatic changes in the variability properties of QSOs with redshift (at a fixed luminosity). First, as the black hole mass of an individual QSO decreases towards higher redshift, the variability will increase as  $\sigma \propto M_{BH}^{0.25}$  (most dramatically at  $z > 2$ ). In addition, because of the evolution in the luminosity function (in this model due to the fading of individual QSOs) one should compare objects which have followed a similar evolutionary path (i.e. the same starting luminosity). The observed evolution in the QSO luminosity function (Boyle et al. 1994) would imply a decline in luminosity by a factor of  $\sim 30$  from  $z = 2$  until the present day. Combining both of these effects, the predicted changes are striking (see Figure 10).

The model predictions are, of course, strongly dependent on the assumed accretion efficiencies, redshift of formation etc., but the generic prediction is a rise in the mean variability (at fixed luminosity) towards higher redshift. Our data do not appear grossly inconsistent with these trends, particularly at the highest luminosities where the high redshift QSOs do indeed show evidence for an upturn (see also Figures 8 & 9). At present, therefore, we cannot, conclusively rule out a long-lived QSO model on the basis of variability evolution. Further measurements are clearly required. In particular, examining variability properties at high redshifts ( $z \sim 3$ ) would provide a conclusive test, where the differences are most striking. This will be possible with Chandra and XMM.

In the alternative model, most galaxies have been through a quasar phase (for perhaps  $10^8$  years) and we expect a similar range of black hole masses at any given epoch. This model is also consistent with the current data, although we note that this would not explain the apparent upturn in the  $\sigma/L_x$  relationship for higher redshift AGN.

**Multiple hotspot model:** In this model, the variability amplitude is determined by the number of independent flares. Hence predictions relating to evolutionary models will depend on the physics of the flaring mechanism. If the number of flares is strictly governed by only the source luminosity, then we expect no difference between the long and short lived evolution models. However it seems plausible that a physically larger emitting region will give rise to a greater number of disconnected, independent emitting regions. Hence the similarity in the variability trends at high and low redshift may also be sufficient to rule out a long-lived evolutionary model.

#### 5.4 Explaining the high luminosity upturn

In Section 4 we found evidence that the local anti-correlation between variability and luminosity does not hold at the highest luminosities. Although further observations are clearly required to test the reality of this feature, we will nevertheless speculate on some possible explanations.

Our results tentatively suggest that this feature is caused by redshift evolution, since while our low redshift QSOs show the same anti-correlation between  $\sigma$  and  $L_x$  as previous studies, the higher redshift sources show very different behaviour. A simple interpretation is that earlier QSOs (at a given luminosity) were powered by less massive black holes compared to local AGN (or alternatively were accreting more efficiently).

On the other hand, if luminosity is the driving parameter



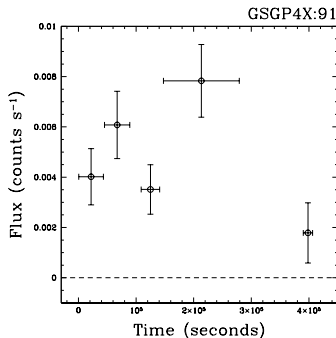


**Figure 11.** Light curve of the variable NELG GSGP4X:091

(rather than redshift evolution) it could reflect an upper limit to the maximum black hole size. Assuming accretion at close to the Eddington limit, the upturn X-ray luminosity ( $5 \times 10^{44}$  erg  $s^{-1}$ ) corresponds to a mass of  $\sim 5 \times 10^7 M_{\odot}$ . This is strikingly similar to the mass at which the space density of active black holes turns over sharply (e.g. see Padovani, Burg & Edelson 1990). This could, in principle, lead to a levelling off in the  $\sigma$  vs.  $L_x$  relationship if we assume (not unreasonably) that there is some scatter in the luminosity for a given black hole size.

## 6 VARIABILITY OF X-RAY LUMINOUS GALAXIES

In recent years, it has become clear from deep X-ray surveys that a population of X-ray luminous narrow emission-line galaxies (NELGs) might provide an explanation for the origin of the cosmic X-ray background (Boyle et al. 1995, Roche et al. 1995, Carballo et al. 1995, Almaini et al 1997, McHardy et al 1998). These galaxies are typically 100 times brighter than normal field galaxies, and appear to have harder X-ray spectra than QSOs (Almaini et al 1996). The nature of this X-ray emission is still controversial, but the presence of massive starburst activity and/or obscured AGN has been postulated.

Here we investigate the X-ray variability of a small number of these galaxies from our Deep *ROSAT* Survey. Unfortunately most of these galaxies are too faint to enable a meaningful variability analysis. Only 6 of the 23 X-ray luminous galaxies presented in Almaini et al (1996) meet the selection criteria outlined in Section 2. A  $\chi^2$  test was performed on these light curves. The null hypothesis of constant flux can only be rejected in the galaxy with highest flux, namely GSGP4X:091, with a significance of  $> 95$  per cent. The light curve is displayed in Figure 11. Such variability clearly favours an AGN origin for the X-ray emission. Applying the maximum likelihood technique, we obtain variability amplitudes  $\sigma = 0.31^{+0.19}_{-0.15}$ , consistent with the typical fluctuations seen in low luminosity AGN (see Figure 5). Combining the light curves of the 5 fainter galaxies, we do not detect a variability amplitude significantly above zero. Formally we obtain a 68 per cent upper limit of  $\sigma < 0.19$ , from which we certainly cannot rule out the presence of AGN-like variability.

## 7 CONCLUSIONS

We have developed a technique for constraining the amplitude of variability in light curves of low signal to noise. By treating each

(normalised) light curve as a ‘snapshot’ from an ensemble, one can obtain a maximum likelihood estimate for the typical variability in the population.

We apply this technique to the light curves of 86 QSOs obtained as part of the Deep *ROSAT* Survey. This represents the first large study of X-ray variability in QSOs over a range in redshift. On timescales of several days, the amplitudes of variability are very similar to those found in very local AGN. We find evidence for trends in the ensemble variability amplitude with both redshift and luminosity. The trend with luminosity is broadly consistent with the anti-correlation seen in local AGN, suggesting that this is the driving parameter rather than redshift.

Unlike local AGN, however, we find evidence for an upturn in the variability at the highest luminosities ( $L_x > 5 \times 10^{44}$  erg  $s^{-1}$ ). We speculate on possible explanations for this upturn. If luminosity is the driving parameter, it could reflect the turn over in the mass spectrum of active black holes. This could also be caused by redshift evolution, e.g. if luminous, high redshift QSOs contain smaller black holes or accrete more efficiently.

Finally, we find evidence for X-ray variability in an object classified as a narrow emission-line galaxy, suggesting the presence of AGN activity.

## ACKNOWLEDGMENTS

We are indebted to Alan Heavens for considerable help with statistical matters, and to Rick Edelson, Niel Brandt and Andy Fabian for useful discussions. OA would also like to thank Seb Oliver, Chris Willott and Dave Alexander for an illuminating (if somewhat drunken) conversation in Bologna.

## REFERENCES

- Abramowicz M.A., Bao G., Lanza A., Zhang X., 1991, *A&A*, 245, 454  
 Almaini O., Shanks T., Boyle B.J., Griffiths R.E., Roche N., Stewart G.C. & Georgantopoulos I., 1996, *MNRAS*, 282, 295  
 Almaini O., Shanks T., Griffiths R.E., Boyle B.J., Roche N., Stewart G.C. & Georgantopoulos I., 1997, *MNRAS*, 291, 372  
 Barr P. & Mushotzky R.F., 1986, *Nature*, 320, 421  
 Boyle B.J., Fong R., Shanks T., Peterson B.A., 1987, *MNRAS*, 277, 717  
 Boyle B.J., Griffiths R.E., Shanks T., Stewart G.C., Georgantopoulos, I., 1994, *MNRAS*, 271, 639  
 Boyle B.J., McMahon R.G., Wilkes B.J., & Elvis M., 1995, *MNRAS* 272, 462  
 Carballo et al. 1995, *MNRAS*, 277, 1312  
 Edelson R., Nandra K., 1999, *ApJ*, 514, 682  
 Georgantopoulos I., Stewart G.C., Shanks T., Griffiths R.E., Boyle B.J., 1996, *MNRAS*, 280, 276  
 Green A.R., McHardy I.M. & Lehto H.J. 1993, *MNRAS* 265, 664  
 Krolik J., Done C., Madejski G., 1993, *ApJ*, 402, 432  
 Lawrence A., Watson M.G., Pounds K.A., Elvis M., 1987, *Nature*, 325, 694  
 Lawrence A. & Papadakis I. 1993, *ApJ* 414, L85  
 McHardy I.M. 1990. In Proc. 23rd ESLAB Symp., ed. J. Hunt, B. Battrick, p. 1111. Paris: Eur. Space Agency  
 McHardy & Czerny 1987, *Nature*, 325, 696  
 McHardy I. et al., 1998, *MNRAS*, 295, 641  
 Mushotzky R.F., Done C., Pounds K.A., 1993, *ARA&A*, 31, 717  
 Nandra K., George I.M., Mushotzky R.F., Turner T.J., Yaqoob T., 1997, *ApJ*, 476, 70  
 Padovani P., Burg R., Edelson R.A., 1990, *ApJ*, 353, 438  
 Plucinsky P.P., Snowden S.L., Briel U.G., Hasinger G., Pfeiffermann E., 1993, *ApJ*, 418, 519  
 Rees M., 1984, *ARA&A*, 22, 471

Roche N., Shanks T., Georgantopoulos I., Stewart G.C., Boyle B.J., & Griffiths R.E., 1995, MNRAS, 273, L15  
 Schmidt M., Schneider D.P., Gunn J.E., 1995, AJ, 110, 68  
 Shanks T., Georgantopoulos I., Stewart G.C., Pounds K.A., Boyle B.J. & Griffiths R.E., 1991, Nat, 353, 315  
 Turner T.J., George I.M., Nandra K., Turcan D., 1999, ApJ, 524, 667

## APPENDIX A: CORRECTING FOR OBSERVATION LENGTH, BINNING AND TIME DILATION

Detailed Fourier analyses of local AGN have revealed larger amplitude fluctuations at low frequencies, parameterised by power spectra of the form:

$$P(f) \propto f^{-\alpha} \quad (\text{A1})$$

where  $\alpha \simeq 1.5$ . Thus the amplitude of variability will depend on the exact range of timescales that we sample. If we sample frequencies in the range  $f_1 < f < f_2$ , the intrinsic variance will relate to the power spectrum as follows ( $\alpha \neq 1$ ):

$$\sigma^2 = \int_{f_1}^{f_2} P(f) df \quad (\text{A2})$$

$$\propto f_1^{1-\alpha} - f_2^{1-\alpha} \quad (\text{A3})$$

One can use this to correct for different sampling by normalising all QSOs to the same frequency range. We adopt a low frequency bound  $f_1$  corresponding to a timescale of 1 week ( $1.65 \times 10^{-6}$  Hz). This reflects the typical observation length in our QSOs. We arbitrarily choose  $f_2 = 10^{-3}$  Hz, corresponding to the length of the shortest bins ( $\sim 1000$ s).

In order to normalise to these frequencies, 3 distinct corrections must be applied to the amplitudes ( $\sigma$ ) derived in Section 3. The largest of these arises because the 7 fields are of differing observation lengths, varying from  $\sim 2$  days for the QSF3 field to a maximum of  $\sim 14$  days for the F864 field. We expect larger amplitude variations for longer integration times. For a total observation length  $T$ , assuming perfect sampling and  $f_1 \ll f_2$ , Equation A2 leads to:

$$\langle \sigma \rangle \propto T^{(1-\alpha)/2} \quad (\text{A4})$$

A second bias arises because of the irregular gaps in the data and from the re-binning described in Section 2. In particular, the bins in many fainter QSOs are merged, which will reduce the observed variance by averaging out high frequency variability. Quantifying these effects would be exceptionally difficult analytically because of the irregular sampling. We therefore carry out simulations for each QSO in order to quantify this behaviour. This is described in detail in Appendix B. For the faintest QSOs with only 2 widely separated bins, we find that these effects produce an average reduction in  $\sigma_Q$  by a factor  $\beta = 1.34$  compared to a perfectly sampled light curve.

Finally a correction may also be applied for the effect of cosmological time dilation. If we sample frequencies in a light curve in the range  $f_1 < f < f_2$  then the intrinsic standard deviation in the light curve will be given by Equation A3. If instead we observe the redshifted frequencies  $f' = f/(1+z)$  then the observed  $\sigma$  will be reduced by approximately  $(1+z)^{-0.25}$ . Thus the amplitude we have measured for QSOs of redshift  $z = 2$  should be increased by a factor  $\sim 1.3$  for comparison with QSOs at zero redshift.

In principle we can correct for each of these effects in order to compare all QSOs within the same frequency range. We therefore normalise all values of  $\sigma_Q$  as follows:

$$\sigma_Q^{norm} = (1+z)^{0.25} \times \beta \times (T_i/week)^{-0.25} \times \sigma_Q^{data} \quad (\text{A5})$$

When combining an ensemble of QSOs, this correction can be included in Equation 7 (simply replace  $\sigma_Q$  with  $\sigma_Q^{data}$  as given above, and solve for  $\sigma_Q^{norm}$  with individual corrections for each QSO). Since these three corrections rely on an assumed form for the power spectrum, which may not be entirely valid for the general QSO population, we also display results based on the raw, uncorrected data for comparison.

## APPENDIX B: SIMULATING LIGHT CURVES

A time process  $x(t)$  may be represented by its Fourier integral:

$$x(t) = \int_{-\infty}^{+\infty} X(f) e^{2\pi i f t} df \quad (\text{B1})$$

The power spectrum of  $x(t)$  is defined as the modulus squared of the inverse Fourier transform (neglecting factors of  $2\pi$ ):

$$P(f) = \left| \int_{-\infty}^{+\infty} x(t) e^{-2\pi i f t} dt \right|^2 = |X(f)|^2 \quad (\text{B2})$$

Rather than assuming random variability (ie. white noise) for the QSOs, we assume that all QSOs show the same power spectra as local Seyfert galaxies, ie.  $P(f) \propto f^{-1.5}$  (McHardy & Czerny 1987, Lawrence & Papadakis 1993). A general theoretical light curve can then be constructed to satisfy this spectral form:

$$x(t) = \int_{-\infty}^{+\infty} |P(f)|^{1/2} e^{i[2\pi f t - \phi(f)]} df \quad (\text{B3})$$

where the real function  $\phi(f)$  represents the phase information lost by the power spectrum method. In a stochastic random process governed by a large number of variables we expect no relation between the phase and frequency of Fourier components, and indeed this has been shown for a number of *EXOSAT* AGN (Krolik, Done & Madejski 1993). The light curves were therefore simulated using a random phase  $\phi(f)$ . Sampling  $x(t)$  over discrete time intervals  $t_k$ , the Fourier integral collapses into the discrete Fourier transform and we obtain:

$$x(t_k) \propto \sum_{f_1}^{f_2} |P(f)|^{1/2} \cos [2\pi f t_k - \phi(f)] \quad (\text{B4})$$

The lowest contributing frequencies are chosen at  $10^{-6}$  Hz. The high frequency cut off (the Nyquist frequency) was chosen at an arbitrarily high value of  $10^{-2}$  Hz, close to the limit of power spectrum observations (Nandra et al 1997). To obtain the required amplitude of variability, the light curves are scaled and a flat d.c. component added to give a total fractional variance of the required amplitude. The resulting light curve is then corrected to allow for the redshift of the QSO (viz. all times multiplied by  $1+z$ ) and a random section is sampled and rebinned in exactly the same way as the real data. 1000 such simulations are carried out for each QSO in order to determine the correction factor,  $\beta$ , which gives the mean change in the intrinsic standard deviation  $\sigma$  as a result of the binning structure:

$$\beta = \sigma_{intrinsic} / \langle \sigma_{binned} \rangle \quad (\text{B5})$$

For the 86 QSOs in our sample, values of this correction factor lie in the range  $1 < \beta < 1.34$  with the largest values for the faintest QSOs with only 2 widely spaced temporal bins.

### APPENDIX C: THE EVOLUTION OF BLACK HOLE MASS IN A LONG-LIVED QSO MODEL

Averaged over an accretion timescale, the luminosity of a QSO relates to its accretion rate via:

$$L(z) = \epsilon \dot{M} c^2 = 5.7 \times 10^{46} \epsilon \left( \frac{\dot{M}}{M_{\odot} \text{yr}^{-1}} \right) \quad (\text{C1})$$

where  $\epsilon$  is the accretion efficiency, taken to be  $\sim 10\%$  after Rees (1984), and  $L$  is the bolometric luminosity emitted across the entire electromagnetic spectrum. For a typical radio quiet quasar the bolometric correction from 0.1 – 2 keV is approximately a factor of 12 from gamma-ray to far infra-red wavelengths.

In the long-lived QSO model, the evolution of the QSO luminosity function (e.g. Boyle et al 1994) directly describes the evolution of individual QSOs:

$$L \propto (1+z)^3 \quad z < 2 \quad (\text{C2})$$

At higher redshifts, studies of optical (and radio) quasars suggest that the luminosity function is roughly flat during the epoch  $2 < z < 3$ , with a rapid decline beyond redshift  $z = 3$  (Schmidt, Schneider & Gunn 1995). For the purposes of a long-lived model, we therefore assume QSOs began accreting at  $z = 3$  and estimate the initial mass of the black hole by assuming that the system began by radiating at the Eddington luminosity (Rees 1984).

$$L_{max} = L_{Edd} \sim 1.3 \times 10^{38} \frac{M(z=3)}{M_{\odot}} \text{ergs}^{-1} \quad (\text{C3})$$

In order to relate the evolution in time with the evolution in redshift, we use the standard relation from a Robertson-Walker metric ( $\Lambda = 0, q_0 = 1/2$ ):

$$t = 2/3 H_0^{-1} (1+z)^{-3/2} \quad (\text{C4})$$

From the above, one can obtain the evolution of mass with redshift:

$$\frac{dM}{dz} = \frac{dM}{dt} \cdot \frac{dt}{dz} \quad (\text{C5})$$

$$= \frac{-H_0 L(z)}{\epsilon c^2} (1+z)^{-5/2} \quad (\text{C6})$$

$$= \frac{-H_0 L_{max}}{27 \epsilon c^2} (1+z)^{1/2} \quad (\text{C7})$$

We can integrate this relation to obtain the mass as a function of  $z$ , where we fix the constant of integration using Equation C3. This is shown in Figure C1. For the  $z < 2$  epoch, this evolution is parameterised as follows:

$$M(z) = \frac{L_{max}}{10^{38}} \left[ 13 + 0.7 \epsilon^{-1} h_{50}^{-1} (5.2 - (1+z)^{3/2}) \right] \quad (\text{C8})$$

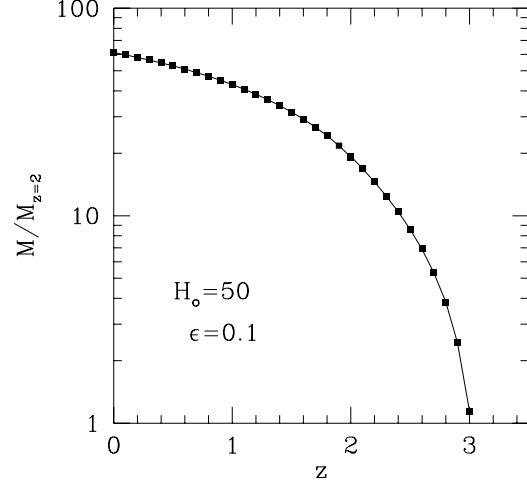


**Figure C1.** Showing the predicted growth in black hole mass from  $z = 3$  until the present day, assuming a long-lived QSO evolution model, with an initial mass given by the Eddington limit.